


RESEARCH

Open Access



Cancer cell-selective induction of mitochondrial stress and immunogenic cell death by PT-112 in human prostate cell lines

R. Soler-Agesta¹, R. Moreno-Loshuertos^{1*}, C. Y. Yim², M. T. Congenie², T. D. Ames², H. L. Johnson³, F. Stossi³, M. G. Mancini³, M. A. Mancini³, C. Ripollés-Yuba¹, J. Marco-Brualla¹, C. Junquera⁴, R. Martínez-De-Mena⁵, J. A. Enríquez⁵, M. R. Price², J. Jimeno^{1,2} and A. Anel^{1*} 

Abstract

PT-112 is a novel immunogenic cell death (ICD)-inducing small molecule currently under Phase 2 clinical development, including in metastatic castration-resistant prostate cancer (mCRPC), an immunologically cold and heterogeneous disease state in need of novel therapeutic approaches. PT-112 has been shown to cause ribosome biogenesis inhibition and organelle stress followed by ICD in cancer cells, culminating in anticancer immunity. In addition, clinical evidence of PT-112-driven immune effects has been observed in patient immunoprofiling. Given the unmet need for immune-based therapies in prostate cancer, along with a Phase I study (NCT#02266745) showing PT-112 activity in mCRPC patients, we investigated PT-112 effects in a panel of human prostate cancer cell lines. PT-112 demonstrated cancer cell selectivity, inhibiting cell growth and leading to cell death in prostate cancer cells without affecting the non-tumorigenic epithelial prostate cell line RWPE-1 at the concentrations tested. PT-112 also caused caspase-3 activation, as well as stress features in mitochondria including ROS generation, compromised membrane integrity, altered respiration, and morphological changes. Moreover, PT-112 induced damage-associated molecular pattern (DAMP) release, the first demonstration of ICD in human cancer cell lines, in addition to autophagy initiation across the panel. Taken together, PT-112 caused selective stress, growth inhibition and death in human prostate cancer cell lines. Our data provide additional insight into mitochondrial stress and ICD in response to PT-112. PT-112 anticancer immunogenicity could have clinical applications and is currently under investigation in a Phase 2 mCRPC study.

Keywords PT-112, Prostate cancer, Immunogenic cell death, Mitochondrial stress, Autophagy

*Correspondence:

R. Moreno-Loshuertos

raquelml@unizar.es

A. Anel

anel@unizar.es

¹Biochemistry and Molecular and Cell Biology, Aragón Health Research Institute (IIS-Aragón), University of Zaragoza, Zaragoza, Spain

²Promontory Therapeutics Inc, New York, NY, USA

³Department of Molecular and Cellular Biology, Integrated Microscopy Core, Baylor College of Medicine, Houston, TX, USA

⁴Anatomy and Human Histology Department, Faculty of Medicine, University of Zaragoza/IIS-Aragón, Zaragoza, Spain

⁵Carlos III National Center for Cardiovascular Research, Madrid, Spain



© The Author(s) 2024. **Open Access** This article is licensed under a Creative Commons Attribution-NonCommercial-NoDerivatives 4.0 International License, which permits any non-commercial use, sharing, distribution and reproduction in any medium or format, as long as you give appropriate credit to the original author(s) and the source, provide a link to the Creative Commons licence, and indicate if you modified the licensed material. You do not have permission under this licence to share adapted material derived from this article or parts of it. The images or other third party material in this article are included in the article's Creative Commons licence, unless indicated otherwise in a credit line to the material. If material is not included in the article's Creative Commons licence and your intended use is not permitted by statutory regulation or exceeds the permitted use, you will need to obtain permission directly from the copyright holder. To view a copy of this licence, visit <http://creativecommons.org/licenses/by-nc-nd/4.0/>.

Background

Prostate cancer is the second leading cause of cancer-associated death among men, with an estimated 34,700 deaths per year in the United States [1]. Over 1.4 million men were diagnosed with the disease in 2020, making it one of the most frequently occurring malignancies leading to mortality in men worldwide [2]. Despite recent improvements in prostate cancer treatment, the development of new therapies is a persistent clinical challenge. Current standard-of-care regimens such as chemotherapy (e.g., docetaxel or cabazitaxel) and androgen-deprivation therapy exhibit toxicity and/or a high incidence of acquired resistance [3–7], and there is an unclear treatment paradigm as disease continues to progress. This is particularly true in late-line mCRPC patients who have already received chemotherapy, hormone therapy, and/or recently approved lutetium-177, leading to limited treatment options [8–10]. Additionally, precision medicine approaches, while resulting in regulatory approval of PARP inhibitors, are generally indicated for 11–13% of the mCRPC population harboring BRCA1/2 mutations [11–13]. Recently, immune checkpoint inhibitor-based approaches such as anti-CTLA-4 and anti-PD-1 antibodies have been successfully used across several different cancer types [14, 15]. However, these agents have not demonstrated robust clinical activity in prostate cancer, with several large Phase 3 studies reporting negative results, likely due to the immunologically cold nature of disease [16–19]. Taken together, there is a high unmet need for novel agents capable of anticancer immune activation, particularly in the late-line setting [8–10, 16, 17].

PT-112 is a novel, immunogenic cell death (ICD)-inducing small molecule currently under Phase 2 clinical development, including in late-line mCRPC [20, 21]. Preliminary evidence of safety, efficacy and clinical benefit in mCRPC was observed for monotherapy and in combination with anti-PD-L1 in two prior dose escalation trials with PT-112 [22–25]. Recent findings have shown evidence of ribosome biogenesis inhibition and nucleolar stress by PT-112 in human cancer cell lines [26]. These early molecular effects, together with organelle stress observed in mitochondria and endoplasmic reticulum in murine cells [27–29] likely contribute to the immunogenicity of PT-112; in preclinical models, it induces ICD via damage-associated molecular pattern (DAMP) release, recruits immune effector cells in the tumor environment, and synergizes with immune checkpoint inhibitors [30]. Immune effects of PT-112 have recently been demonstrated in a Phase 2 study in patients with thymic epithelial tumors [31, 32].

In addition, PT-112 is distributed to multiple tissues and organs, including kidney, lung and liver, with the highest concentrations found in bone, likely driven by the pyrophosphate moiety [33]. This suggests PT-112 may

provide benefit to patients with prostate cancer, a population with a high incidence of bone metastases [34] and where immune checkpoint inhibitors have not been demonstrated to be effective, highlighting a need for novel immune-based therapies.

Our previous studies using L929 mouse tumor cell lines with well-characterized metabolic features showed mitochondrial stress upon PT-112 treatment, as demonstrated by mitochondrial reactive oxygen species (mtROS) accumulation and changes in the mitochondrial membrane potential [28]. These PT-112-induced effects, along with cell death, were more pronounced in cell lines with mitochondrial DNA mutations, dependence on glycolysis for survival, and higher in vivo tumorigenic and metastatic potential [35]. These data suggested the relevance of mitochondria to PT-112-induced cell death.

Mitochondria are essential organelles as a hub for metabolic, bioenergetic, redox, and apoptotic signaling pathways, and thus play a key role in tumor cell proliferation [36]. Mitochondrial stress has been shown to facilitate pro-tumorigenic metabolic reprogramming in malignant cells, and basal levels of mtROS are commonly higher in cancer compared to healthy cells [37–39]. However, driving mitochondrial stress and mtROS levels beyond a certain threshold can lead to unmanageable oxidative stress and ultimately cell death [36, 38]. These observations suggest that novel therapeutic approaches harnessing the unique metabolic profile of cancer cells can promote antitumor activity and cancer cell death through the induction of a mitochondrial stress response.

Given PT-112 activity observed in prostate cancer patients, as well as previously reported mitochondrial stress induction by PT-112 in mouse tumor cells, we explored the effects of PT-112 in a panel of human prostate cell lines. Here, we report: (1) cancer cell selectivity; (2) cell death characterization; (3) mitochondrial stress features such as mtROS generation, compromised membrane integrity and changes in morphology; (4) ICD induction via DAMP release; and lastly, (5) evidence of autophagy. Together, this work aims to advance the understanding of a key organelle stress contributing to PT-112's activity and its resulting anticancer immunity in prostate cancer.

Methods

Cell culture

Human prostate cell lines were maintained according to ATCC recommendations. PC-3, DU-145, and VCap were cultured in high glucose DMEM medium with GlutaMAX (Life Technologies, Paisley, UK). LNCap and 22Rv1 were cultured in RPMI 1640 medium (Life Technologies, Paisley, UK). LNCap-C4 and LNCap-C4-2 were cultured in a mixture of DMEM: F12 (4:1) supplemented with biotin (4.9 ng/mL), adenine (251.8 ng/mL), insulin (0.1 ng/

mL), and transferrin (88.6 ng/mL). RWPE-1 (immortalized, non-tumorigenic human prostate cell line) was cultured in Keratinocyte-SFM supplemented with EGF human recombinant (5 ng/mL) and bovine pituitary extract (50 µg/mL) (Gibco, Grand Island, NY, USA). All cell culture media used for prostate cancer cell lines were supplemented with 10% fetal calf serum, penicillin (1000 U/mL) and streptomycin (10 mg/mL) (PanBiotec, Aid-enbach, Germany). Cells were incubated at 37 °C and 5% CO₂ using standard procedures. PC3, LNCap, VCap, and RWPE-1 cell lines were kindly provided by Dr. M. Jesús Vicent from CIPF, Valencia, while DU-145, LNCap C4, LNCap C4-2 and 22Rv1 cell lines were a kind gift of Dr. Santiago Ramón y Cajal from Hospital Vall d'Hebron (Barcelona). LNCap and DU-145 cells used for confocal fluorescence microscopy work were purchased from ATCC and routinely tested for mycoplasma contamination by DAPI staining and high magnification imaging.

Cell viability assays

Relative cell growth in response to PT-112 compared to control, untreated cells was measured using Mossman's method (i.e., MTT assay). Briefly, 2×10^4 cells were seeded per well in a 96-well flat-bottom plate and incubated with increasing concentrations of PT-112 (2, 6, and 10 µM) for 24–72 h (h) at 37 °C. Subsequently, 10 µL of a 5 mg/mL MTT solution was added to each well and incubated for 3 h at 37°C. During incubation, viable cells reduced the MTT solution to insoluble purple formazan crystals, which were then solubilized with a mixture of isopropanol and 0.05 M HCl. Finally, absorbance was measured by a microplate reader (Dynatec, Pina de Ebro, Spain).

Cytotoxicity assays and cell death quantification

Cytotoxicity was measured as follows: 2×10^4 cells were seeded per well in a 96-well plate and incubated with increasing concentrations of PT-112 (2, 6, and 10 µM) for 24–72 h at 37 °C. Cell death in untreated and treated cells was analyzed by flow cytometry using a FACSCalibur flow cytometer (BD Biosciences, Madrid, Spain) after simultaneous incubation with annexin-V-FITC and 7-AAD (BD Biosciences, Madrid, Spain) in annexin binding buffer (140 mM NaCl, 2.5 mM CaCl₂, 10mM HEPES/NaOH, pH 7.4) for 10 min (min).

Analysis of caspase-3 activation

Caspase-3 activation was measured using a FITC-labelled antibody against cleaved caspase-3 (BD Pharmingen™, Madrid, Spain). For this purpose, 1×10^5 LNCap-C4 and DU-145 cells pretreated with 10 µM of PT-112 for 24–72 h were fixed with 4% paraformaldehyde solution for 15 min at 4 °C. Then, cells were washed with PBS buffer, permeabilized using a 0.1% saponin dilution

supplemented with 5% fetal bovine serum, and incubated for 15 min at room temperature (RT). After washing, samples were incubated with the antibody for 30 min at RT and analyzed by flow cytometry using a FACSCalibur flow cytometer (BD Biosciences, Madrid, Spain).

Cell morphology assessments

2×10^4 cells (DU-145, LNCap, or PC-3) were treated with or without 10 µM of PT-112 for 72 h. Images were taken using an inverted microscope (Nikon Eclipse TE300). For cell morphology assessments using transmission electron microscopy (TEM), refer to *Transmission Electron Microscopy (TEM)*.

Apoptosis and necroptosis inhibition assays

2×10^4 cells (LNCap-C4 and DU-145) were seeded in a 96-well plate and incubated with pan-caspase inhibitor Z-VAD-fmk (50 µM; MedChem Express, New Jersey, USA) and/or RIPK-1 inhibitor necrostatin-1 (30 µM; MedChem Express, New Jersey, USA) for 1 h. Cells were then treated with 10 µM of PT-112 and incubated for 48 h at 37 °C. Both inhibitors were refreshed in their corresponding wells after 24 h. Finally, cell death was assessed via flow cytometry using a FACSCalibur flow cytometer (BD Biosciences, Madrid, Spain) after 10 min incubation with annexin-V-FITC and 7-AAD (Sigma, Madrid, Spain) in annexin binding buffer (140 mM NaCl, 2.5 mM CaCl₂, 10mM HEPES/NaOH, pH 7.4).

mtROS, mitochondrial mass and mitochondrial membrane potential measurements

Total mtROS production, mitochondrial mass, and mitochondrial membrane potential were each measured using a FACSCalibur flow cytometer (BD Biosciences, Madrid, Spain) in prostate cells with or without 10 µM PT-112 for 24–72 h. For mtROS production and mitochondrial mass, cells were incubated at 37 °C with 5 µM MitoSOX™ (ThermoFisher, Rockford, IL, USA) for 30 min or 300 nM MitoTracker™ green staining (Invitrogen) for 15 min, respectively. To measure alterations in mitochondrial membrane potential, DU-145 and LNCap-C4 cells were simultaneously incubated with 20 nM TMRE (Molecular Probes, Madrid, Spain) and annexin-V-DY-634 (Sigma, Madrid, Spain) for 30 min at 37 °C.

Confocal fluorescence microscopy was used to visualize mitochondrial membrane polarization. 2×10^3 cells (LNCap and DU-145) per well were plated in an optical plastic bottom 384-well plate (Aurora Microplates, Scottsdale, AZ, USA) and, after overnight attachment, treated with control buffer or 25 µM PT-112 for 72 h. Cells were then stained live with Hoechst 33,342 (ThermoFisher, Rockford, IL, USA #62249, 1:5000 dilution) and either TMRE (ThermoFisher, Rockford, IL, USA #T669, 1:1000 dilution) or JC-1 (ThermoFisher, Rockford,

IL, USA #T3168, 1:1000 dilution) for 30 min. Next, cells were imaged on a Yokogawa CV8000 high-throughput spinning disk confocal using a 20x/1.0 water objective capturing a 10 μm z-stack in 9 fields of view per condition. Images were then projected at maximum intensity for quantification. Image analysis was performed using the CellPathfinder software (Yokogawa, Sugar Land, TX, USA). Briefly, nuclei were identified using the Hoechst channel, followed by a dilation step to include the mitochondrial signal ("virtual cell") from where intensity-based measurements were extracted. The experiment was repeated three independent times with four technical replicates per biological replicate.

OXPPOS performance and metabolism measurements

Oxygen consumption rate (OCR) measurements of 30,000 LNCap-C4 cells treated with or without 10 μM PT-112 for 24 h were performed using the Seahorse XF Cell Mito Stress Test Kit and the XF96 Extracellular Flux Analyzer (Seahorse Biosciences, Lexington, MA, USA). Cells were incubated in Seahorse media (1mM pyruvate, 2mM glutamine, 1 M glucose at pH 7.4) for 30 min at 37°C without CO_2 . According to the manufacturer's instructions, OCR was measured in basal conditions and after sequential addition of oligomycin (CV inhibitor), FCCP (respiration and ATP synthesis uncoupler), and rotenone+antimycin A (AA+Rot, CI and CIII inhibitors, respectively). OCR data were normalized to the number of viable cells as determined by the CyQuant Cell Proliferation Assay (Thermo Fisher, Rockford, IL, USA).

Energy maps were constructed using the XF96 Extracellular Flux Analyzer (Seahorse Biosciences, Lexington, MA, USA) per the manufacturer's instructions. The energetic phenotype of LNCap-C4 cells was determined based on measurements of OCR and extracellular acidification rate (ECAR) indicative of OXPPOS and glycolysis, respectively, in untreated, control cells and following 10 μM PT-112 treatment for 24 h.

Mitochondria purification

Mitochondria were purified as previously described [40]. Briefly, 2×10^7 cells were centrifuged, washed twice with PBS, and frozen at -80 °C for 24 h. Pellets were resuspended in a volume of a hypotonic buffer (MOPS 10mM, sucrose 83 mM, pH 7.2) equal to 7 \times the cell pellet volume and incubated on ice for 2 min. Samples were then homogenized using a Potter-Dounce homogenizer with a Teflon piston, and 8 to 10 strokes were performed. After adding an equal volume of a hypertonic buffer (MOPS 30 mM, 250 mM, pH 7.2), the samples were centrifuged at 1000 $\times g$ for 5 min at 4 °C, and only the supernatants were centrifuged again at 11,000 $\times g$ for 2 min at 4 °C. Finally, mitochondria-containing pellets were washed with media A (Tris 10 mM, EDTA 1 mM, saccharose 0.32 M, pH 7).

Protein extraction

A total of 5×10^6 cells were lysed with 100 μL of lysis buffer (1% Triton-X-100, 150 mM NaCl, 50 mM Tris/HCl pH 7.6, 10% v/v glycerol, 1 mM EDTA, 1 mM sodium orthovanadate, 10 mM sodium pyrophosphate, 10 $\mu\text{g}/\text{mL}$ leupeptin, 10 mM sodium fluoride, 1 mM methyl phenyl sulfide; Sigma, St. Louis, MO, USA) for 30 min on ice. The mixture was ultra-centrifugated at 12,000 rpm for 20 min at 4 °C. The supernatant was analyzed using the BCA assay (Thermo Fisher, Rockford, IL, USA) for determining protein concentration and mixed with 3 \times loading buffer (SDS 3% v/v, 150 mM Tris/HCl, 0.3 mM sodium molybdate, 30% v/v glycerol, 30 mM sodium pyrophosphate, 30 mM sodium fluoride, 0.06% p/v bromophenol blue, 30% v/v 2-mercaptoethanol; Sigma, St. Louis, MO, USA).

Blue native electrophoresis and immunoblot analysis

Separation of respiratory complex (CI, CII, CIII, CIV and CV) and supercomplex proteins in mitochondrial extracts was performed using blue native electrophoresis in a gel gradient according to the published methodology [41, 42]. Briefly, samples were loaded in NativePAGE™ 3–12% Bis-Tris Gel (Invitrogen, Waltham, MA, USA) and run at 100 V for the first 30 min, then at 300 V and 15 mA for the next 3 h. For protein separation of protein extracts, SDS-PAGE (6% and 12% polyacrylamide gel) was used.

Following either method, proteins were transferred to PVDF membranes using semi-dry electrotransfer (GE Healthcare, Chicago, IL, USA). Membranes were blocked with TBS-T buffer (Tris/HCl 10mM, pH 8; NaCl 0.12 M; Tween-20 0.1%, thimerosal 0.1 g/L; Sigma, St. Louis, MO, USA) containing 5% skimmed milk. Protein detection was performed by immunoblot using specific antibodies (Invitrogen, Waltham, MA, USA) against the individual complexes of the mitochondrial electron transport chain: CI (anti-NDUFA9; #459100), CII (anti-SDHA; #459200), CIII (anti-Uqcrc1; #459140), CIV (anti-COI; 459600), and CV (anti- α -F1-ATPase; #459240). Other proteins detected by immunoblot were p62 (Santa Cruz, Dallas, TX, USA, #SC-28359), LC3BI/II (Sigma, Madrid, Spain, #L7543) and HIF-1 α (Novus, Littleton, CO, USA, #NB100–479). Primary antibodies were incubated overnight at 4 °C in agitation. Afterwards, anti-mouse (Sigma, Madrid, Spain, #A9044) or anti-rabbit (Sigma, Madrid, Spain, #A9169) secondary antibodies labeled with peroxidase were incubated for 1 h at RT. Blots were analyzed with Pierce ELC Western Blotting Substrate (Thermo Scientific, Rockford, IL, USA) using Amersham Imager 680 (GE Healthcare Life Sciences, Chicago, IL, USA). Protein expression was quantified by densitometry using ImageJ software. β actin levels were used as a reference to normalize data (Cell Signaling, Danvers, MA, USA, 3700).

Enzymatic activity analysis of respiratory complexes

Purified mitochondria from DU-145 cells treated with or without 10 μM PT-112 for 24 h were used to assess enzymatic activity of respiratory complexes via spectrophotometric quantification as previously described [43]. Briefly, activity of individual complexes and super-complexes was measured using a spectrophotometer (Fisher Scientific; Alcobendas, Spain) based on the following: CI (NADH-dehydrogenase) activity via oxidation of NADH at 340 nm, CII (succinate dehydrogenase) activity via reduction of 2,6-dichlorophenolindophenol at 600 nm, CIV (cytochrome c oxidase) activity via oxidation of cytochrome c at 550 nm, CI+III (NADH cytochrome c oxidoreductase) via reduction of cytochrome c at 550 nm when NADH is added, and CII+III (succinate cytochrome c oxidoreductase) activity via reduction of cytochrome c at 550 nm when succinate is added.

Transmission electron microscopy (TEM)

Samples for TEM were prepared as follows: 5×10^4 DU-145 cells were seeded overnight in an 8-well Nunc™ Lab-Tek® Chamber Slide™ (Thermo, Rockford, IL, USA). Cells were treated with 10 μM PT-112 for 1, 6, 24 and 48 h, and after incubation, the medium was removed. Cells were carefully washed 3 \times for 2 min with 0.1 M PBS at RT and a solution containing 2.5% glutaraldehyde in 0.1 M phosphate buffer (PB; $\text{Na}_2\text{HPO}_4 + \text{NaH}_2\text{PO}_4$ 4:1, pH 7.4) was added. The chamber slide was then incubated at 37 °C for 5 min. The glutaraldehyde solution was refreshed and the chamber slide was again incubated for additional 2 h at 4°C. It was subsequently washed 4 \times (5 min each) with 0.1 M PB before adding a solution of 0.05% NaN_3 in 0.1 M PB and storing the chamber slide at 4°C. For the fixation process, samples were washed 5 \times (5 min each) with PBS and incubated with 2% OsO_4 in PB for 1 h. Next, 3 washes (5 min each) with cold distilled water were performed and samples were dehydrated with increasing concentrations of ethanol (30%, 50% and 70%). Then, samples were stained with 2% uranyl acetate in 70% ethanol for 2 h 30 min. Finally, samples were dehydrated a second time with increasing concentrations of ethanol (70%, 96%, 100%), and then gradually transferred to a 100% epoxy resin, and incubated overnight for their inclusion in resin. The next day, 3 changes of epoxy resin were performed (30 min each), and samples were embedded in the molds with epoxy resin and dried in the oven for 48–72 h at 70 °C. Finally, ultrafine 50 nm cuts were performed and stained with Reynol's solution. Images were taken using a transmission electron microscope (JEOL 1010) at 80 kV.

DAMP emission

ATP secretion was quantified using the luciferase-based ENLITEN ATP Assay (Promega) per the manufacturer's

recommendations via a fluorometer (Biotek) using the supernatant of cells treated with or without 10 μM PT-112 collected at 48 h. Calreticulin (CALR) exposure on the cell surface upon incubation with or without 10 μM PT-112 (48 h) was analyzed by flow cytometry using the Attune NxT flow cytometer (Thermo Fisher Scientific; Branchburg, NJ, USA). Following treatment, cells were washed and stained with Zombie Aqua™ Fixable Viability Kit (BioLegend, San Diego, CA, USA) for 15 min. Subsequently, cells were washed with PBS and incubated with the calreticulin (D3E6) XP® rabbit monoclonal antibody PE Conjugate (Cell Signaling, Danvers, MA, USA, #19780S) in PBS+0.5% BSA (FACs buffer) for 25 min at 4 °C in the dark. Afterwards, cells were washed with FACs buffer and fixed (eBioscience™ Intracellular Fixation & Permeabilization Buffer Set, Invitrogen, Carlsbad, CA, USA) for 30 min at 4 °C in the dark. Then, the supernatant was discarded by centrifugation and cells were incubated with the permeabilization buffer (eBioscience™ Intracellular Fixation & Permeabilization Buffer Set, Invitrogen, Carlsbad, CA, USA) for 5 min. Finally, the supernatant was discarded again by centrifugation and cells were resuspended in FACs buffer for its subsequent analysis. Zombie Aqua™ positive cells (i.e., dead cells) were excluded from the analysis.

Cyto-ID® analysis and autophagosome formation measurement

For autophagy analysis, the autophagosome formation after treatment with PT-112 was evaluated using a Cyto-ID® probe (Enzo Life Sciences, Farmingdale, NY, USA). Cells treated with or without 10 μM of PT-112 for 48–72 h were incubated with 1 μL of Cyto-ID® dye for 30 min at 37 °C. Subsequently, cells were washed with PBS and analyzed by flow cytometry via a FACSCalibur flow cytometer (BD Biosciences, Madrid, Spain).

Statistical analysis and data processing

Statistical analysis was performed using GraphPad Prism (GraphPad Software Inc.). For quantitative variables, results are shown as mean \pm standard error of the mean (SEM). Statistical significance was evaluated using Student's t-test and two-way ANOVA uncorrected Fisher's LSD. Differences were considered significant when $p < 0.05$. Data obtained by flow cytometry were analyzed using FlowJo 10.0.7 (Tree Star Inc., Ashland, OR, USA).

Results

PT-112 selectively inhibits cell growth and causes cell death in prostate cancer cells, but not in non-tumorigenic epithelial prostate cells

We tested differential sensitivity to PT-112 in vitro across a panel of human prostate cancer cell lines (LNCap, LNCap-C4, LNCap-C4-2, DU-145, 22Rv1, VCap, PC-3)

and the non-tumorigenic prostate cell line (RWPE-1). First, we evaluated the ability of PT-112 to inhibit cell growth at increasing concentrations (2, 6, 10 μ M) and incubation times (24, 48 and 72 h) via the MTT assay. Selected PT-112 concentrations represent clinically relevant doses successfully used in previous in vivo experiments [23, 44].

PT-112 inhibited cell growth of prostate cancer cell lines with varying degrees, without appreciably affecting that of the non-tumorigenic cell line RWPE-1 (Fig. 1). In addition, cell death induced by PT-112 was analyzed by flow cytometry using annexin-V-FITC and 7-AAD staining, as described in our previous report using murine fibroblast tumor cell lines [28]. Consistent with the growth inhibition data, PT-112 caused cancer cell death while healthy RWPE-1 cells were largely unaffected after 48–72 h PT-112 treatment (Fig. 2A). Overall, PT-112 was broadly active across the prostate cancer cell lines tested, while sparing benign prostate cells, demonstrating PT-112 cancer cell selectivity.

Next, we further explored PT-112-induced cell death in select cell lines that were especially sensitive to PT-112. DU-145 cells treated with PT-112 followed by simultaneous staining with annexin-V-FITC and 7-AAD were analyzed by flow cytometry. We observed a prominent apoptotic population (annexin-V⁺/7-AAD⁻) in response to PT-112 at 48 h (29.8%) and 72 h (44.1%), with an eventual increase in double-positive stained (i.e., dead) cells

(annexin-V⁺/7-AAD⁺) at 72 h, potentially indicative of secondary necrosis (Fig. 2B).

PT-112 induces caspase-3 activation

Given the emergence of the apoptotic population in response to PT-112, we next analyzed the activation of an apoptosis effector, caspase-3. Caspase-3 activation in DU-145 and LNCap-C4 cells treated with PT-112 for 24, 48, and 72 h was measured by flow cytometry using an antibody specific for cleaved caspase-3. As shown in Fig. 3A and B, the levels of cleaved caspase-3 increased in a time-dependent manner upon PT-112 treatment, reaching as high as 85% and 100% caspase-3 activation at 72 h compared to control in LNCap-C4 and DU-145 cells, respectively. Moreover, PT-112-treated cells showed features of cells undergoing apoptosis, such as plasma membrane blebbing, as well as nuclear and cell fragmentation in apoptotic bodies (Fig. 3C).

To further investigate cell death in PT-112-treated cells, we pretreated LNCap-C4 and DU-145 with the pan-caspase inhibitor, Z-VAD-fmk, and/or the RIPK-dependent necroptosis inhibitor, necrostatin-1. In LNCap-C4, only Z-VAD-fmk caused a significant decrease in cell death following PT-112 treatment. Co-pretreatment of both inhibitors versus Z-VAD-fmk alone resulted in a comparable reduction in cell death in response to PT-112. In DU-145, we observed inhibition of PT-112-induced cell death with Z-VAD-fmk (where % cell death was

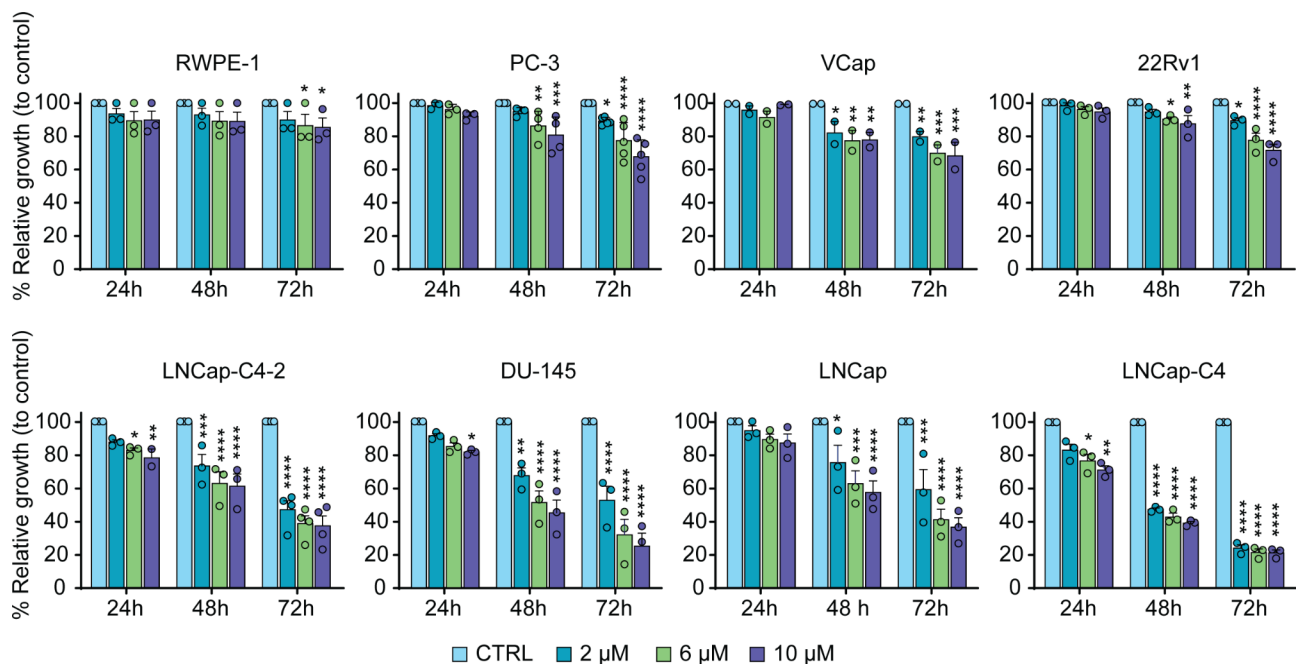


Fig. 1 Relative cell growth (%) upon PT-112 treatment compared to untreated control (CTRL) cells. Cell lines were incubated with increasing concentrations of PT-112 (2, 6, and 10 μ M) for 24–72 h. Cell growth was measured by the MTT assay. Results are shown as a mean \pm SEM of at least 3 independent experiments performed in duplicate. * $p \leq 0.05$, ** $p \leq 0.01$, *** $p \leq 0.001$, **** $p \leq 0.0001$

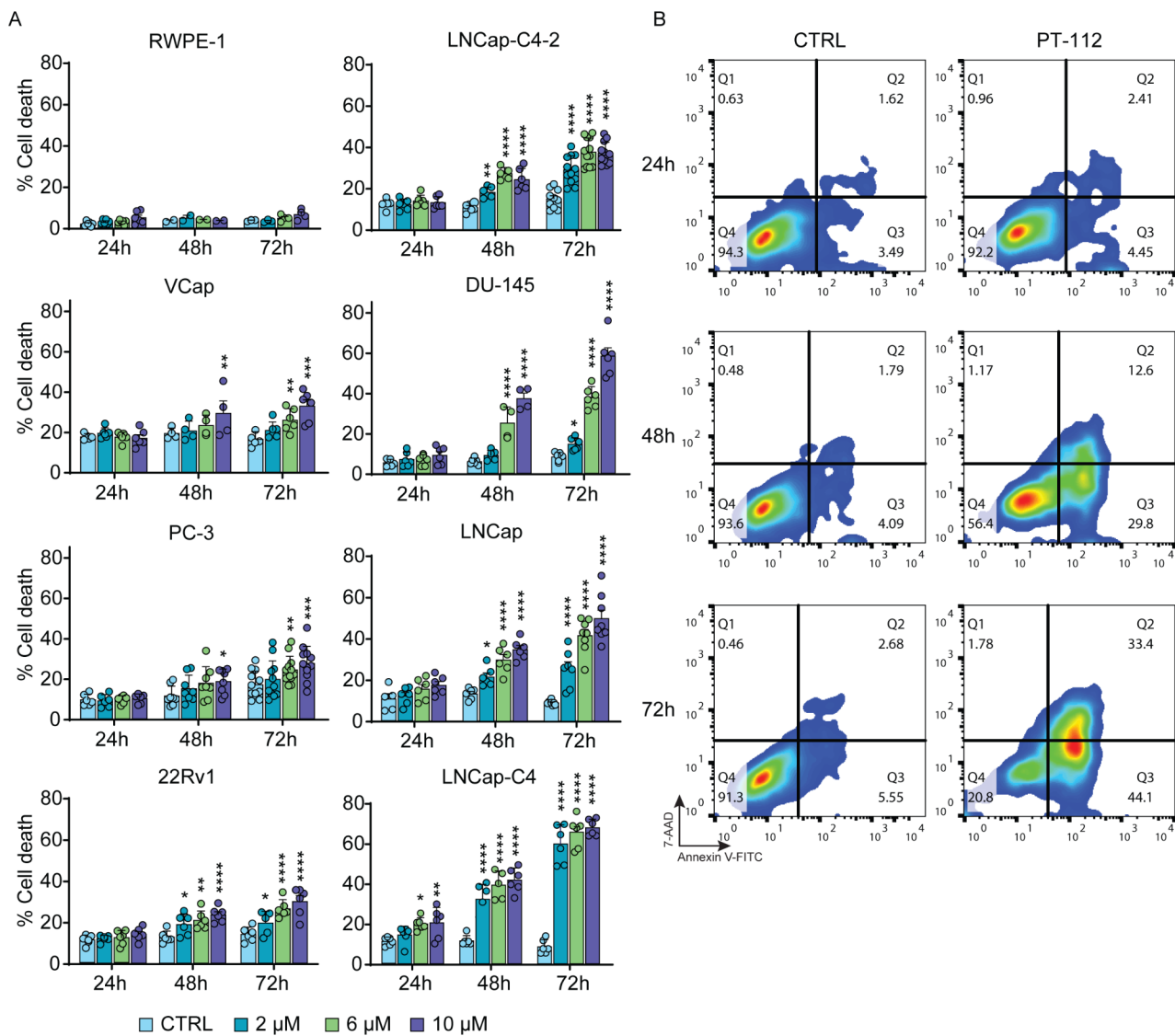


Fig. 2 Relative cell death (%) upon PT-112 treatment compared to untreated control (CTRL) cells. **(A)** Cells were incubated with increasing concentrations of PT-112 (2, 6, and 10 μM) for 24–72 h. Cells were then simultaneously stained with annexin-V-FITC and 7-AAD and analyzed by flow cytometry. Results are shown as mean \pm SEM of at least 3 independent experiments performed in duplicate. * $p \leq 0.05$, ** $p \leq 0.01$, *** $p \leq 0.001$, **** $p \leq 0.0001$. **(B)** Cell death over 72 h PT-112 treatment in DU-145 cells. Representative dot-plots showing the 7-AAD and annexin-V-FITC staining evolution with time of DU-145 cells treated with 10 μM PT-112 for 24–72 h compared to untreated control (CTRL) cells

comparable to that of untreated cells), and to a lesser degree with necrostatin-1 (Fig. 3D).

PT-112 induces mitochondrial stress

Based on our previous work illustrating PT-112 sensitivity in the transformed murine fibroblast cell lines with mitochondrial deficiencies [28], we investigated different mitochondrial parameters in human prostate cancer cells treated with PT-112. As shown in Figs. 4A and 10 μM PT-112 treatment for 48–72 h increased mtROS production in all cancer cell lines, but not in the healthy prostate cell line RWPE-1, in line with the selective growth inhibition and cytotoxicity data in Figs. 1 and 2. Notably,

LNCap-C4 and DU-145 cells exhibited pronounced increases in mtROS levels compared to untreated cells after 72 h PT-112 treatment (Fig. 4B). Furthermore, PT-112 induced a significant increase in mitochondrial mass at 48 and 72 h (Fig. 4C). Again, PT-112 was broadly active, inducing mitochondrial stress across the cancer cell lines, which exhibit varying basal mitochondrial features (Supplementary Fig. 2A).

Next, we analyzed the effect of PT-112 on mitochondrial membrane potential ($\Delta\psi_m$) in DU-145 and LNCap-C4 cells by flow cytometry using double TMRE and annexin-V-DYE-634 staining, allowing for simultaneous quantification of $\Delta\psi_m$ and cell death, respectively. In

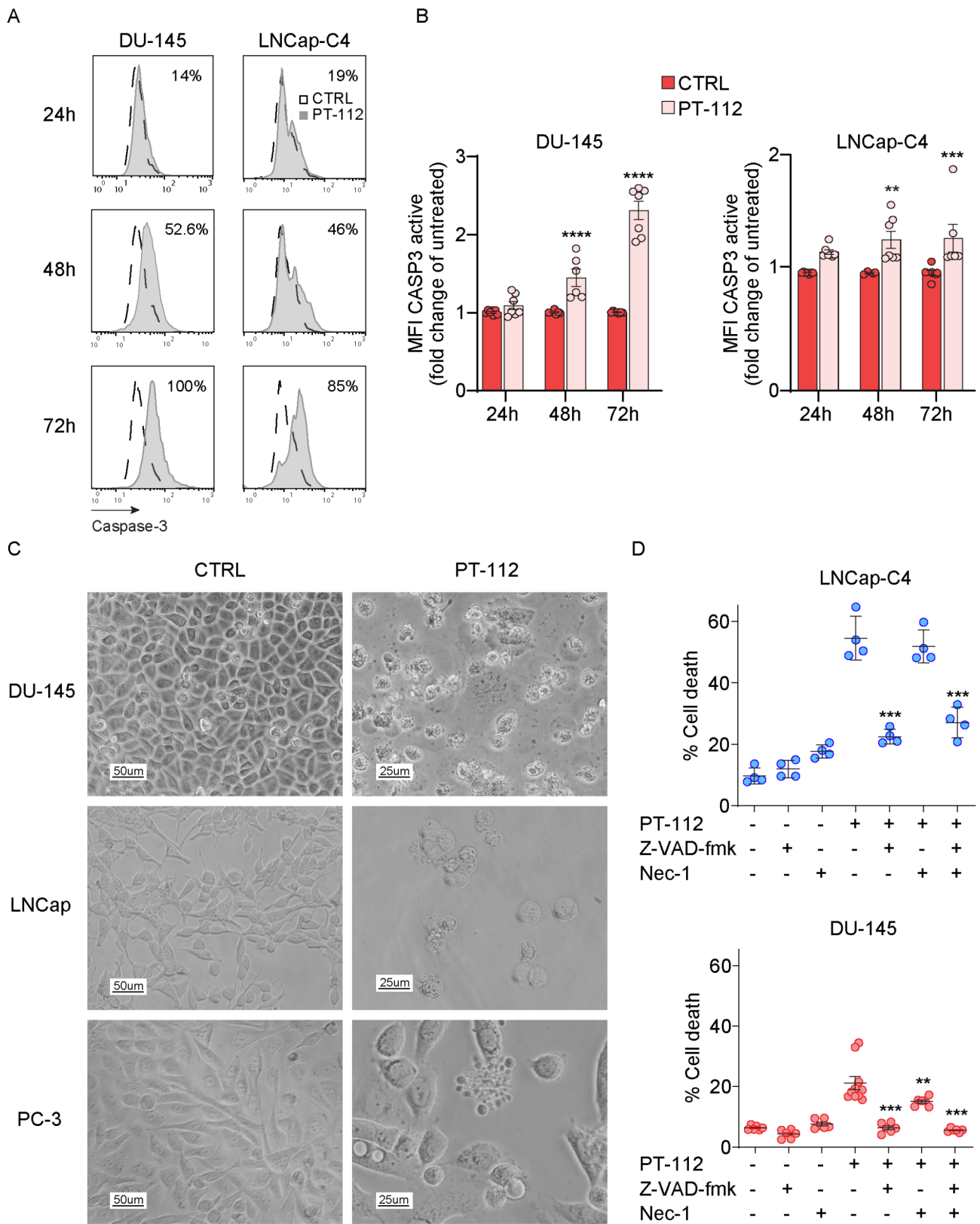


Fig. 3 (See legend on next page.)

(See figure on previous page.)

Fig. 3 Characterization of cell death induced by PT-112 in human prostate cancer cells **(A)** Levels of caspase-3 activation upon PT-112 treatment in DU-145 and LNCap-C4. Cells were treated with 10 μM of PT-112 for 24–72 h, incubated with anti-cleaved caspase-3 labeled with FITC dye, and analyzed by flow cytometry. The numbers in each box represent the percentage of cleaved caspase-3 compared to untreated control (CTRL) cells. **(B)** Quantification of levels of caspase-3 activation. Results are shown as mean \pm SEM of 3 independent experiments performed in duplicate. ** $p \leq 0.01$, *** $p \leq 0.001$, **** $p \leq 0.0001$. **(C)** Representative images of cells treated with 10 μM PT-112 for 72 h were taken using an inverted microscope. **(D)** Effects of Z-VAD-fmk and/or necrostatin-1 (Nec-1) inhibitors on PT-112-induced-cell death. Cells were pretreated for 1 h with or without pan-caspase and/or necroptosis inhibitors and incubated with 10 μM of PT-112 for 48 h. Flow cytometry analysis was performed using annexin-V-FITC and 7-AAD staining. Results are shown as mean \pm SEM of at least 2 independent experiments performed in duplicate. Statistical significance compared to cells treated with PT-112 only is depicted in the graphics. ** $p \leq 0.01$, *** $p \leq 0.001$

both cell lines, PT-112 decreased $\Delta\psi_m$ at 48 h and 72 h of incubation in a time-dependent manner (Fig. 5A). Interestingly, in LNCaP-C4, this decrease in $\Delta\psi_m$ was accompanied by cell death (see Q1) starting at 48 h of PT-112 treatment. In contrast, DU-145 exhibited a cell population that was positive for annexin-V-DYE-634, but still had normal $\Delta\psi_m$ (see Q2), and it was only at 72 h that cells began losing their $\Delta\psi_m$.

We further investigated the effects of PT-112 on $\Delta\psi_m$ using confocal fluorescence microscopy to visualize mitochondrial membrane polarization. LNCap and DU145 cells were treated with vehicle or 25 μM PT-112 for 72 h and stained with the nuclear dye Hoechst and a mitochondrial dye, either TMRE or JC-1. TMRE staining intensity indicates the degree of mitochondrial membrane polarization, while a red-to-green shift in the JC-1 staining indicates a reduction in mitochondrial membrane potential. In both cell lines, clear evidence of mitochondrial membrane depolarization was observed, as indicated by diminished TMRE intensity and by the green shift in the JC-1 stain (Fig. 5B). Together, these results demonstrate that PT-112 reduces mitochondrial membrane polarization, contributing to mitochondrial dysfunction.

PT-112 alters mitochondrial respiration

We next evaluated the effects of PT-112 on mitochondrial respiration and the activity of respiratory complexes in the electron transport chain (ETC). We analyzed the oxygen consumption rate (OCR) and the extracellular acidification rate (ECAR) after 24 h of PT-112 treatment in LNCap-C4, indicating the rates of respiration and glycolysis, respectively. Using cellular respiration modulators oligomycin, FCCP, and rotenone/antimycin A, we assessed key parameters related to mitochondrial respiration and observed compromised mitochondrial function in PT-112-treated cells compared to untreated cells (Fig. 6A). Specifically, relative to control cells, PT-112 caused reductions in (1) basal respiration, (2) ATP-linked oxygen consumption (as shown by the reduction in the OCR upon oligomycin addition), and (3) the spare respiratory capacity (SRC) (as shown by the increase in the OCR relative to basal respiration upon FCCP addition) (Fig. 6A and B), all of which point to mitochondrial dysfunction [45, 46]. In addition, we generated

“energy maps” to compare shifts in cellular metabolic programs in response to PT-112. In line with the results above, PT-112 decreased oxygen consumption (Fig. 6C). Interestingly, PT-112 simultaneously reduced glycolysis as indicated by a decrease in ECAR, shifting cells from being “energetic” (i.e., utilizing OXPHOS and glycolysis) to “quiescent” (i.e., utilizing both metabolic pathways to a lesser degree), indicative of reductions in ATP across these two major pathways.

Additionally, we characterized the basal protein expression of respiratory complexes and supercomplexes within the ETC in the cell line panel, which showed differential metabolic phenotypes (Supplementary Fig. 2B). We further investigated respiratory complexes in DU-145. The activity of specific complexes (CI, CII, and CIV) and supercomplexes (CI+CIII and CII+CIII) was measured after PT-112 treatment via spectrophotometric quantification in mitochondrial extracts and compared to untreated control cells. PT-112 treatment for 24 h significantly reduced the activity of CI and CIV, as well as increased the activity of supercomplexes involving CIII, with no notable effects on CII (Fig. 6D). Given that CIII respiratory complexes contribute to ROS production [47, 48], this increase in the activity of CIII-containing supercomplexes in response to PT-112 may explain mtROS generation (see Fig. 4).

PT-112 causes morphological changes in mitochondria

In order to further assess the effects of PT-112 on mitochondria, we analyzed cell and organelle morphology of DU-145 treated with PT-112 via TEM at different time points. Overall, after brief exposure as short as 1 h, PT-112 caused changes in mitochondrial morphology, electron density, and size; modifications to and loss of cristae; and breakage of mitochondrial membranes, and these effects became more pronounced over time (Fig. 7). Moreover, autophagic vacuole formation was observed, especially in the vicinity of mitochondria, suggesting an active mitochondrial autophagic process, or mitophagy [49], in response to PT-112. In addition to mitochondrial morphological changes, evidence of increased cytoplasmic complexity and features of apoptosis were seen, as expected.

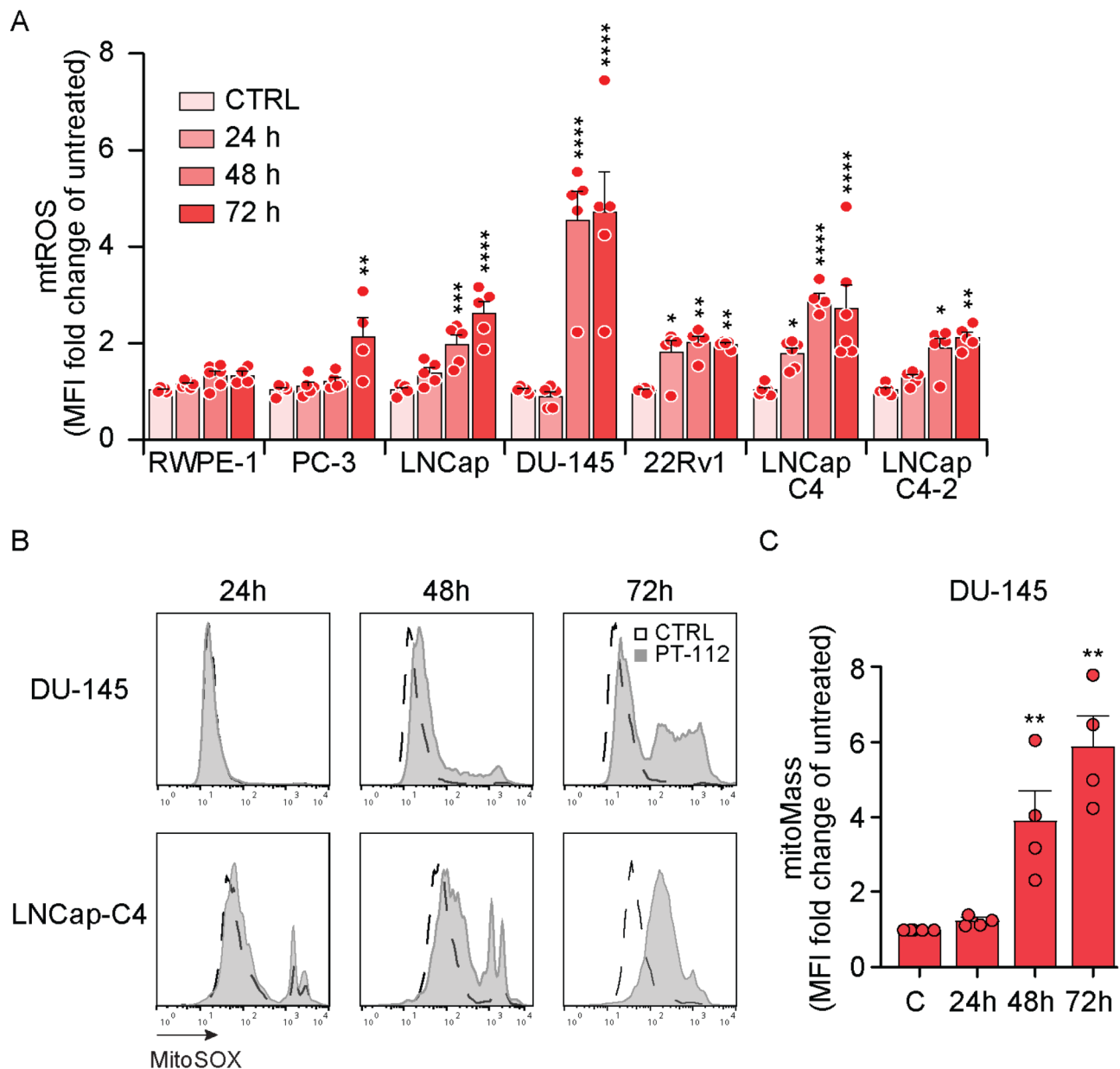


Fig. 4 Effects of PT-112 on mtROS production and mitochondrial mass in human prostate cancer cell lines. **(A)** mtROS levels in cells treated with 10 μ M PT-112 for 24–72 h were analyzed by flow cytometry using MitoSOX™ labeling. Graph bars correspond to mean fluorescence intensity (MFI) normalized to untreated control (CTRL) cells. Results are shown as mean \pm SEM from 3 independent experiments. * $p \leq 0.05$ ** $p \leq 0.01$, *** $p \leq 0.001$, **** $p \leq 0.0001$. **(B)** Representative histograms showing mtROS production in DU-145 and LNCap-C4. Dotted histograms correspond to the fluorescence of untreated control (CTRL) cells, and gray-colored histograms correspond to the fluorescence values of treated cells. **(C)** Mitochondrial mass (mitoMass) was measured by flow cytometry using MitoTracker™ Green in DU-145 upon 10 μ M PT-112 incubation for 24, 48, and 72 h. Graph bars correspond to mean fluorescence intensity (MFI) normalized to CTRL. Results are shown as mean \pm SEM from 3 independent experiments. ** $p \leq 0.01$

PT-112 induces DAMP release associated with ICD

Given the anticancer immunogenicity of PT-112 demonstrated in mouse *in vitro* and *in vivo* models [24, 28, 30, 44], we tested the ability of PT-112 to induce DAMP emission in human prostate cancer cell lines. We assessed ATP release and CALR exposure on the cell surface, both of which are immunostimulatory DAMPs essential for ICD [50]. Consistent with the prior findings, PT-112

caused ATP release in LNCap-C4, 22Rv1 and DU-145 cells (Fig. 8A). On the other hand, CALR exposure was clearly detected in DU-145, but not in LNCap-C4 or 22Rv1 cells at this time point, possibly due to cell line-specific responses to PT-112 (Fig. 8B).

ICD has been linked to autophagy [51], and we previously reported the initiation of autophagy by PT-112 in transformed murine fibroblast cell lines [28]. This is

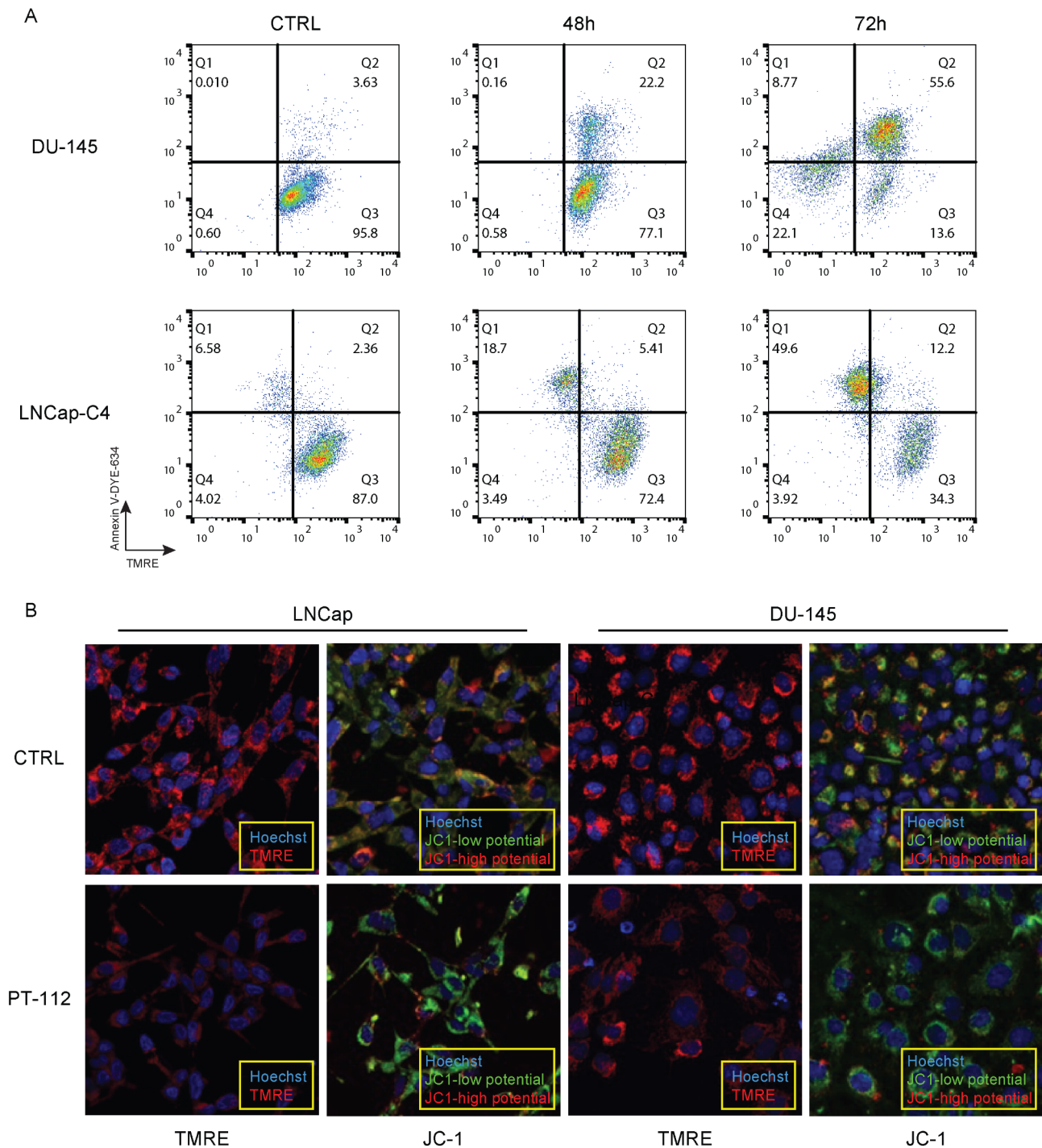


Fig. 5 Effects of PT-112 on mitochondrial membrane potential ($\Delta\psi_m$) in human prostate cancer cell lines. **(A)** Mitochondrial membrane potential was monitored by flow cytometry using simultaneous TMRE and annexin-V-DYE-634 staining in DU-145 and LNCap-C4 treated with 10 μ M PT-112 for 48 h and 72 h. The series of dot plots show the staining evolution of the treated cell population compared to the control (CTRL). **(B)** Confocal fluorescence microscopy images correspond to mitochondrial staining of LNCap and DU-145 cell lines with TMRE or JC-1, with or without 25 μ M PT-112 treatment for 72 h. Nuclei were stained using Hoechst dye

consistent with the evidence of PT-112-induced mitophagy observed via TEM in Fig. 7. Based on these data, we set out to investigate autophagosome formation using the Cyto-ID[®] method. As shown in Fig. 9, PT-112

induced autophagosome formation across the tested cell lines (with the exception of LNCap cells), demonstrating autophagy initiation. In most of these cell lines, autophagosome formation was observed as early as 24 h,

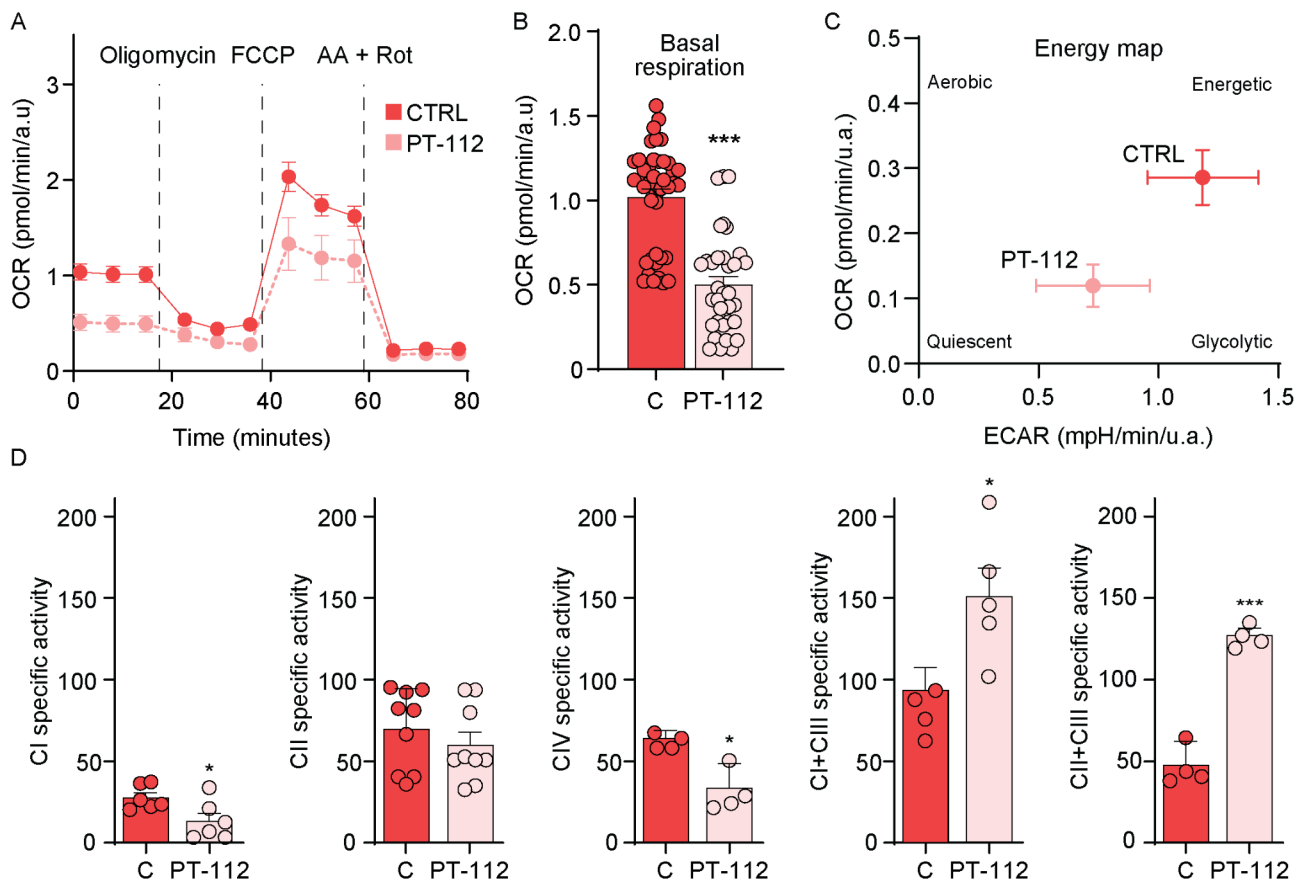


Fig. 6 Effects of PT-112 on mitochondrial respiration and activity of respiratory complexes and supercomplexes in the ETC. **(A)** OCR and ECAR were measured in LNCap-C4 cells treated with vehicle (CTRL) or 10 μ M PT-112 for 24 h. Dotted vertical lines indicate administration of injections of the specified cellular respiration modulators at different time points, such that basal respiration (i.e., OCR prior to oligomycin injection), ATP-linked oxygen consumption (the difference between basal OCR and oligomycin-inhibited OCR) and spare respiratory capacity (the difference between FCCP-induced maximal OCR and basal OCR) were investigated. Results are expressed as mean \pm SEM at each time point. **(B)** Graph bars quantifying basal respiration measured in Fig. 6A. Results are expressed as mean \pm SEM from multiple experiments. *** $p \leq 0.001$. **(C)** Energy map plotting OCR (indicative of OXPHOS) vs. ECAR (indicative of glycolysis) for cells treated with vehicle (CTRL) or 10 μ M PT-112 for 24 h. Four relative bioenergetic phenotypes (aerobic vs. glycolytic and energetic vs. quiescent) are labeled. Note that the axes for OCR in **(A)** and **(C)** utilize arbitrary units (a.u.), and thus are not comparable. **(D)** Bar graphs show the activity of respiratory complexes and supercomplexes in DU-145 cells treated with 10 μ M PT-112 for 24 h. Results are expressed as mean \pm SEM from at least 4 independent experiments. * $p \leq 0.05$, *** $p \leq 0.001$

with DU-145 and PC-3 exhibiting evidence of autophagy through 72 h of PT-112 treatment. LNCap-C4 cells showed reduced autophagosome formation at 72 h relative to 24 h, where the level dropped below that seen in control cells. These data demonstrate that PT-112 clearly activates autophagy in most prostate cancer cell lines, though each cell line likely follows a different time course.

Discussion

This is the first demonstration of PT-112's broad preclinical anticancer effects as well as its ability to induce ICD and mitochondrial stress in human prostate cancer cells, in line with clinical evidence of PT-112 activity observed in mCRPC patients [22, 23]. Specifically, using a panel of human prostate cancer cell lines, the present study demonstrates the ability of PT-112 to (1) cause growth

inhibition and death in cancer cells without affecting non-tumorigenic epithelial prostate cells, (2) promote mitochondrial stress in cancer cells, as evidenced by mtROS generation and disruptions in mitochondrial membrane potential, respiration and morphology, (3) activate autophagy, and lastly, (4) induce ICD.

The selective growth inhibition and cytotoxicity, as well as mitochondrial stress induction by PT-112 observed in prostate cancer cells, but not in non-tumorigenic prostate cells, was consistent with our prior data in the murine L929 system, where those cell lines with a higher degree of in vivo tumorigenicity and metastatic potential exhibited a higher sensitivity to PT-112 [28, 35]. This selectivity may explain PT-112's general safety and tolerability observed in clinical studies [21, 24, 25, 31, 32, 52]. It is interesting to note that PT-112 was active across different

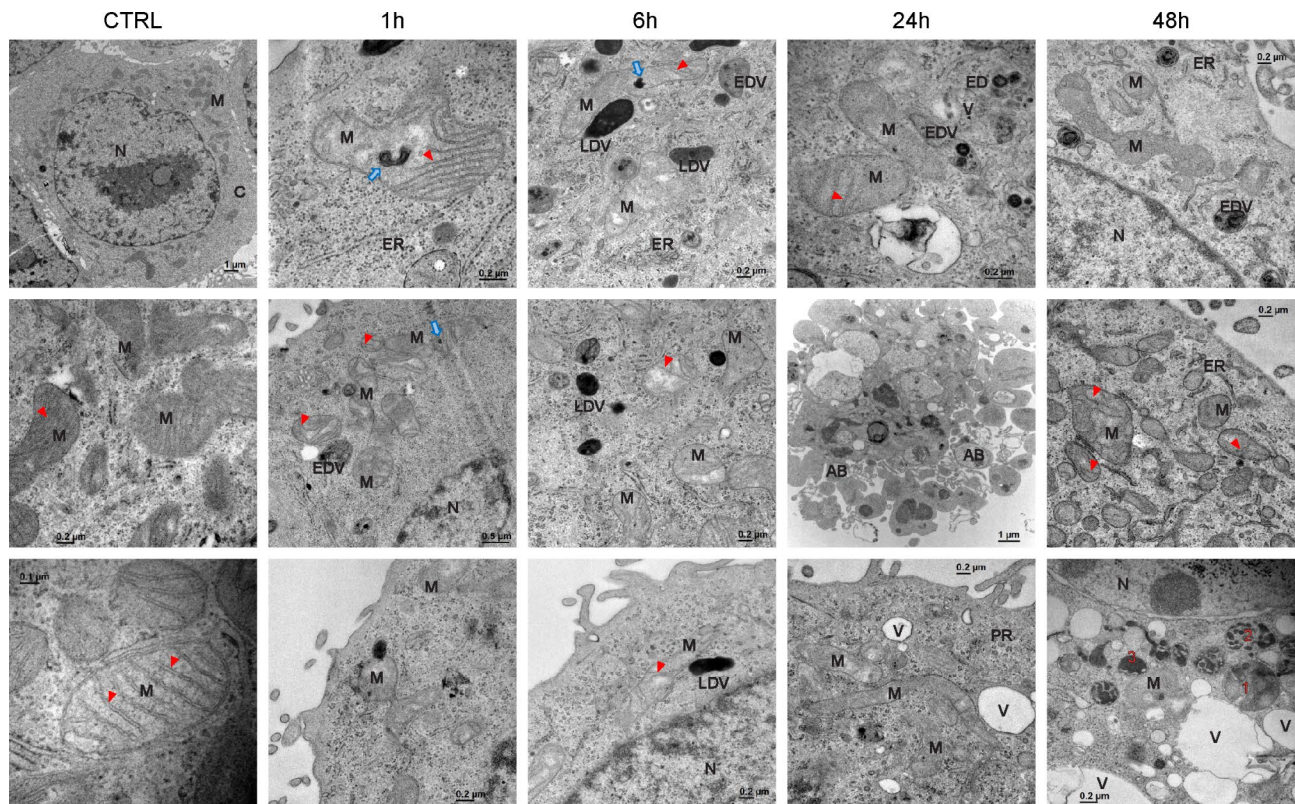


Fig. 7 Effects of PT-112 on cell and organelle morphology in DU-145 cells treated with vehicle (CTRL) or 10 μ M PT-112 for 1, 6, 24 and 48 h. Representative TEM images at the indicated resolution are shown. Letters and symbols indicate the following. **Red arrows:** mitochondria cristae, **blue arrows:** accumulation of degraded membranes inside the mitochondrial matrix, **PR:** Polyribosome, **C:** Cytoplasm, **M:** Mitochondria, **N:** Nucleus, **AB:** Apoptotic Body, **EDV:** Early Degradation Vesicle (secondary lysosome), **LDV:** Late Degradation Vesicle (late lysosome), **ER:** Endoplasmic Reticulum, **V:** low electron density vacuole. Red numbers in the right bottom image (48 h time) illustrate sequential stages of a possible mitophagy process

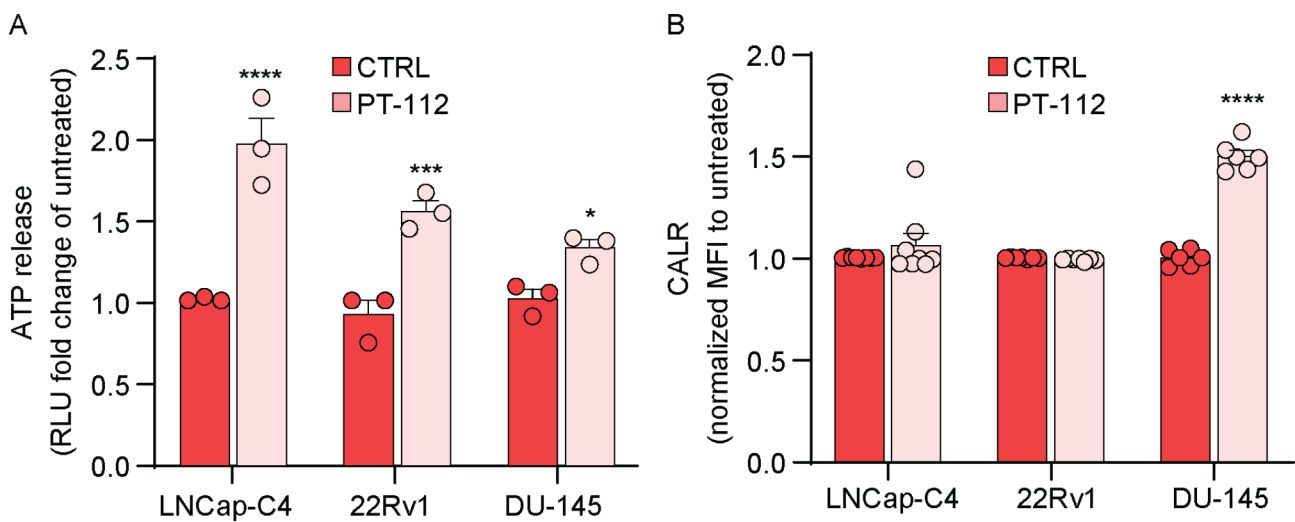


Fig. 8 DAMP emission induced by PT-112 in human prostate cancer cell lines. **(A)** ATP release and **(B)** calreticulin exposure upon 10 μ M PT-112 treatment for 48 h. Bar graphs show relative measurements for each parameter normalized to untreated control (CTRL) samples. Results are expressed as mean \pm SEM from 3 independent experiments. RLU: relative light units. * $p < 0.05$, *** $p < 0.001$, **** $p < 0.0001$

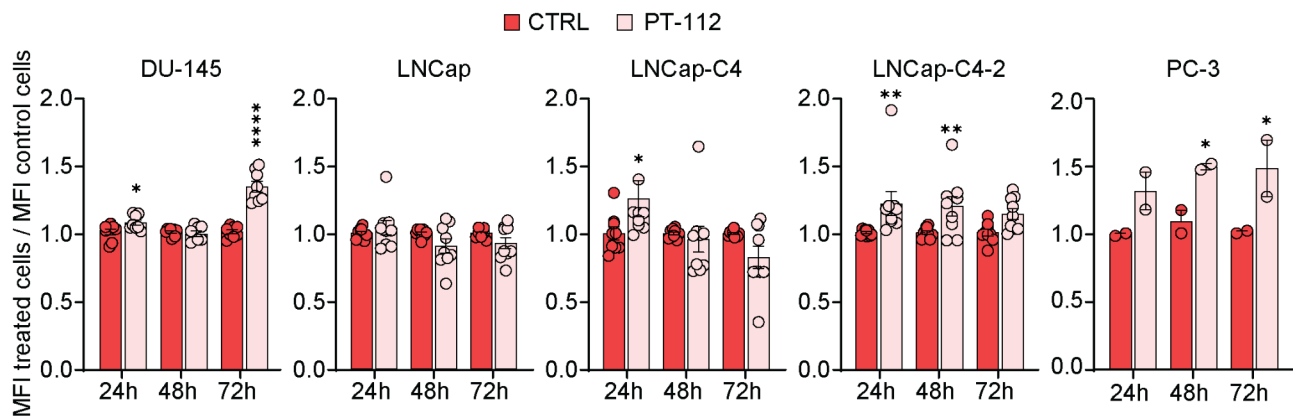


Fig. 9 Autophagy induction by PT-112. Analysis of autophagosome formation. Cells were incubated with 10 μ M of PT-112 for 24–72 h. The autophagosome formation was analyzed by flow cytometry using the Cyto-ID[®] method. Bars represent the mean fluorescence intensity (MFI) of treated cells compared to untreated control cells (CTRL). Results are expressed as mean \pm SEM from 3 independent experiments with technical duplicates for all cell lines except in PC-3 cells, where the mean \pm SEM is calculated from 2 independent experiments. * $p \leq 0.05$, ** $p \leq 0.01$, **** $p \leq 0.0001$

prostate cancer cell lines exhibiting varying basal mitochondrial features and mutational status, suggesting broad clinical application in prostate cancer, especially the late-line setting where the disease is highly heterogeneous [3–5, 53]. Moreover, the evidence of apoptosis and ICD in PT-112-treated cells raises an intriguing question of how these biochemical events could be observed simultaneously. Caspase-3-dependent apoptosis was previously thought to be an immunologically silent event; however, there is emerging evidence that it neither precludes ICD nor contradicts evidence of anticancer immunity [54]. Apoptotic cells can release DAMPs and ultimately undergo ICD in certain conditions [54]. It is interesting to note that, in contrast to what was observed here in human prostate cancer cells, PT-112-induced cell death in murine L929-derived cell lines did not rely on the activity of caspase-3. Nevertheless, evidence of ICD induction via DAMP release was clearly observed in both L929-derived [28] and human prostate cancer cell lines, though possible differences in kinetics for release of individual DAMPs may exist across different cell lines. This suggests that while varying cell death mechanisms are possible, the ability of PT-112 to induce ICD remains consistent across all the cell lines tested and may be a more universal feature of PT-112's mechanism.

Our findings clearly demonstrate that PT-112 causes mitochondrial stress and DAMP release in prostate cancer cells. Given the link between these two events reported in the literature, it is plausible that these effects observed in PT-112-treated cells may be directly related, contributing to an anticancer immune response. For example, upon mitochondrial stress and damage, mitochondria have been shown to promote not only mtROS generation, but also the release of ICD-associated DAMPs such as ATP [55, 56].

Our data also show the ability of PT-112 to affect autophagic flux (e.g., autophagosome formation, autophagic degradation of proteins etc.), which may stem from mitochondrial stress, given mitochondria are the major source of ROS required for autophagy induction [51, 57, 58]. Additionally, recent studies have reported a link between the initiation of autophagy and the release of ATP, promoting ICD [51, 59]. Increased extracellular ATP can also lead to cancer cell death by contributing to mitochondrial membrane damage and caspase-3-dependent apoptosis in tumor cells [51], suggesting bidirectionality and/or crosstalk in this process. While the precise mechanisms through which mitochondrial stress leads to ICD in response to PT-112 are to be investigated, it is likely that PT-112-driven mitochondrial stress contributes to ICD induction via mtROS generation and DAMP release, the latter of which can be further stimulated upon autophagy initiation.

Lastly, this work reinforces the ability of PT-112 to induce organelle stress, adding to the recent finding that PT-112 caused ribosome biogenesis inhibition and nucleolar stress as early as 6 to 8 h post-treatment in vitro [26]. These events have been reported to contribute to downstream organelle stresses, including mitochondrial stress. During nucleolar stress, nucleolar proteins such as NPM1 translocate to the nucleoplasm and interact with mitochondrial proteins, causing mitochondrial stress and release of mitochondrial DNA (mtDNA) into the cytosol, potentially activating the innate immune system via cGAS/STING [60–64]. Interestingly, mtDNA release has been observed in PT-112-treated cancer cells [27]. Disrupted ribosome biogenesis has also been shown to upregulate autophagy [65], which is linked to ICD as described above, and can have broad impacts on protein translation that likely play a role in driving organelle stress. Moreover, this disruption could explain PT-112's

selectivity to cancer cells observed here. Cancer cells have increased demand for ribosome biogenesis in the nucleolus compared to normal cells due to high proliferation rates and associated need for protein generation [66, 67], potentially rendering them more sensitive to ribosome biogenesis disruption by PT-112.

Conclusions

In the evolving treatment landscape of mCRPC, there remains a need for novel therapies with anticancer immune effects. PT-112 is a promising small molecule with a mechanism of action selective to cancer cells, causing organelle stress and ICD. Taken together, our data provide additional insight into mitochondrial stress and ICD in response to PT-112, and how these effects culminate in anticancer immunity. PT-112 anticancer immunogenicity could in part explain previous clinical observation of durable responses extending beyond the treatment duration [24] and immune effects demonstrated in a small cohort of human patients [31, 32]. In addition, the broad activity of PT-112 in prostate cancer cells coupled with its differentiated mechanism from the current standards of care could help address the high unmet need in late-line mCRPC. PT-112 monotherapy is currently under investigation in a Phase 2 study with mCRPC patients who have exhausted standard of care options [20]. Future work will further characterize and identify key components facilitating PT-112-induced mitochondrial stress and explore connections with ICD and ribosome biogenesis inhibition.

Abbreviations

ICD	Immunogenic cell death
mCRPC	Metastatic castration-resistant prostate cancer
DAMP	Damage-associated molecular pattern
mtROS	Mitochondrial reactive oxygen species
mtDNA	Mitochondrial DNA
TEM	Transmission Electron Microscopy
CALR	Calreticulin
$\Delta\psi_m$	Mitochondrial membrane potential
ETC	Electron transport chain
OCR	Oxygen consumption rate
ECAR	Extracellular acidification rate

Supplementary Information

The online version contains supplementary material available at <https://doi.org/10.1186/s12967-024-05739-x>.

Supplementary Material 1: Supplementary Fig. 1. Basal mitochondrial characterization of human prostate cancer cell lines and the non-tumorigenic prostate cell line RWPE-1. (A) Graph bars correspond to mean fluorescence intensity (MFI) normalized to the non-tumorigenic cell line RWPE-1. The ratio of mtROS levels to mitochondrial mass was calculated and normalized to that of RWPE-1. Results are shown as a mean \pm SEM of at least 3 experiments. (B) Protein expression of respiratory complexes and supercomplexes (SCs) was first normalized to Complex V then compared to healthy prostate cell line RWPE-1. The numbers represent the summed expression level of the indicated complex protein found as a monomer or within a SC. Complex and SC composition are annotated in the figure, with unresolved SC bands labeled as CI-SC (left) and CIII-SC (right)

Acknowledgements

The authors would like to acknowledge Dr. Santiago Ramón y Cajal and Anna Santamaría, Vall d'Hebron Institute of Oncology, Barcelona; Dr. M^a Jesús Vicent, Centro de Investigación Príncipe Felipe, Valencia, for prostate cancer cell lines and the use of Servicio General de Apoyo a la Investigación-SAI at Universidad de Zaragoza.

Author contributions

RSA has conceived the work, acquired, analyzed and interpreted most of the experimental data, drafted and revised substantially the work and approved the submitted version; RML has conceived the work, acquired, analyzed and interpreted the experimental data related with mitochondria, substantially revised the work and approved the submitted version; CYY has helped to conceive the work, substantially revised the work and approved the submitted version; MTC substantially revised the work and approved the submitted version; TDA has helped to conceive the work, substantially revised the work and approved the submitted version, HLJ, FS, MGM and MAM have acquired, analyzed and interpreted data related with confocal microscopy, revised the work and approved the submitted version; CRY has acquired, analyzed and interpreted experimental data and approved the submitted version; JMB has helped to acquire, analyze and interpret experimental data related with mitochondria metabolism, revised the work and approved the submitted version; CJ has helped to acquire, analyze and interpret experimental data related with transmission electron microscopy, revised the work and approved the submitted version; RMM and JAE have helped to acquire, analyze and interpret experimental data related with Seahorse technology, revised the work and approved the submitted version; MRP and JJ have contributed to the conception of the work, revised the work and approved the submitted version; AA has conceived the work, coordinated the completion of the experimental work, analyzed and interpreted the experimental data, drafted and revised substantially the work and approved the submitted version.

Funding

This work was mainly supported by Promontory Therapeutics Inc. and it was also partially supported by project PID2019-105128RB-I00 financed by MCIN/AEI/655 <https://doi.org/10.13039/501100011033/> and "FEDER Una manera de hacer Europa". The work of RSA was supported by the grant from the Asociación Española Contra el Cáncer (AECC) PRDAR21487SOLE. High throughput imaging and analysis was possible via support from the Center for Advanced Microscopy and Image Informatics (CAMII, CPRI170719) and the Integrated Microscopy Core at Baylor College of Medicine (funding from NIH (DK56338, CA125123, ES030285, S10OD030414).

Data availability

The datasets used and/or analysed during the current study are available from the corresponding author on reasonable request.

Declarations

Ethics approval and consent to participate

Not applicable.

Consent for publication

Not applicable.

Competing interests

C.Y. Yim, M. Congenie, T.D. Ames, M.R. Price and J. Jimeno are or have been employees of Promontory Therapeutics Inc.

Received: 6 August 2024 / Accepted: 7 October 2024

Published online: 11 October 2024

References

1. Siegel R, Miller K, Wagle N, Jemal A. Cancer statistics, 2023. *CA Cancer J Clin*. 2023;73:17–48.
2. Sung H, Ferlay J, Siegel R, Laversanne M, Soerjomataram I, Jemal A, Bray F. Global Cancer statistics 2020: GLOBOCAN estimates of incidence and Mortality Worldwide for 36 cancers in 185 countries. *CA Cancer J Clin*. 2021;71:209–49.

3. Buck S, Koolen S, Mathijssen R, de Wit R, van Soest R. Cross-resistance and drug sequence in prostate cancer. *Drug Resist Update*. 2021;56:100761.
4. Galletti G, Leach B, Lam L, Tagawa S. Mechanisms of resistance to systemic therapy in metastatic castration-resistant prostate cancer. *Cancer Treat Rev*. 2017;57:16–27.
5. Hwang C. Overcoming docetaxel resistance in prostate cancer: a perspective review. *Ther Adv Med Oncol*. 2012;4:329–40.
6. Parker C, Castro E, Fizazi K, Heidenreich A, Ost P, Procopio G, Tombal N, Gillissen S. AI E: prostate cancer: ESMO Clinical Practice guidelines for diagnosis, treatment and follow-up. *Ann Oncol*. 2020;31:1119–34.
7. Sandhu S, Moore C, Chiong E, Beltran H, Bristow R, Williams S. Prostate cancer. *Lancet*. 2021;398:1075–90.
8. Chazan G, Anton A, Wong S, Shapiro J, Weickhardt A, Azad A, Kwan E, Spain L, Gunjur A, Torres J, et al. Beyond cabazitaxel: late line treatments in metastatic castration resistant prostate cancer: a retrospective multicentre analysis. *Asian-Pacific J Clin Oncol*. 2022;18:642–9.
9. Turco F, Gillessen S, Cathomas R, Buttigliero C, Vogl U. Treatment Landscape for patients with castration-resistant prostate Cancer: patient selection and unmet clinical needs. *Res Rep Urol*. 2022;14:339–50.
10. Shore N, Ionescu-Iltu R, Laliberté F, Yang L, Lejeune D, Yu L, Duh M, Mahendran M, Kim J, Ghote S. Beyond Frontline Therapy with Abiraterone and Enzalutamide in Metastatic Castration-resistant prostate Cancer: a real-world US Study. *Clin Genit Cancer*. 2021;19:480–90.
11. Valsecchi A, Dionisio R, Panepinto O, Paparo J, Palicelli A, Vignani F, Di Maio M. Frequency of germline and somatic BRCA1 and BRCA2 mutations in prostate Cancer: an updated systematic review and Meta-analysis. *Cancers*. 2023;15:2435.
12. Lukashchuk N, Barnicle A, Adelman C, Armenia J, Kang J, Barrett J, Harrington E. Impact of DNA damage repair alterations on prostate cancer progression and metastasis. *Front Oncol*. 2023;26:1162644.
13. Al-Akhras A, Chehade C, Narang A, Swami U. PARP inhibitors in metastatic castration-resistant prostate Cancer: unraveling the therapeutic Landscape *Life* 2024;14:198.
14. Sanmamed MF, Chen L. A paradigm shift in Cancer Immunotherapy: from enhancement to normalization. *Cell*. 2018;175:313–26.
15. Sharma P, Allison J. The future of immune checkpoint therapy. *Science*. 2015;348:56–61.
16. Cha H, Lee J, Ponnazhagan S. Revisiting immunotherapy: a focus on prostate Cancer. *Cancer Res*. 2020;80:1615–23.
17. Runcie K, Dallos M. Prostate Cancer Immunotherapy—finally in from the Cold? *Curr Oncol Rep*. 2021;23:88.
18. Serrano-Del Valle A, Naval J, Anel A, Marzo I. Novel forms of Immunomodulation for Cancer Therapy. *Trends Cancer*. 2020;6:518–32.
19. Lanka S, Zorko N, Antonarakis E, Barata P. Metastatic castration-resistant prostate Cancer, Immune checkpoint inhibitors, and Beyond. *Curr Oncol*. 2023;30:4246–56.
20. Bryce A, Karp D, Tagawa S, Nordquist L, Rathkopf D, Adra N, Dorff T, Baeck J, O'Donnell J, Ames T, et al. A phase 2 study of immunogenic cell death inducer PT-112 in patients with metastatic castration-resistant prostate cancer. *J Clin Oncol*. 2023;41(Suppl 6):TPS292.
21. Imbimbo M, Ghisoni E, Mulvey A, Bouchaab H, Mederos-Alfonso N, Karp D, Camidge D, Mansfield A, Yim C, Ames T, et al. A phase IIa study of the novel immunogenic cell death (ICD) inducer PT-112 plus avelumab (PAVE) in advanced non-small cell lung cancer (NSCLC) patients. *Immuno-Oncol Technol*. 2022;16(Suppl 1):125P.
22. Bryce A, Dronca R, Costello B, Aparicio A, Subudhi S, O'Donnell J, Jimeno J, Yim C, Price M, Karp D. A phase 1b study of novel immunogenic cell death inducer PT-112 plus PD-L1 inhibitor avelumab in metastatic castrate-resistant prostate cancer (mCRPC) patients. *J Clin Oncol*. 2021;39:e17025.
23. Bryce A, Dronca R, Costello B, Infante J, Ames T, Jimeno J, Karp D. PT-112 in advanced metastatic castrate-resistant prostate cancer (mCRPC), as monotherapy or in combination with PD-L1 inhibitor avelumab: findings from two phase I studies. *J Clin Oncol*. 2020;38.
24. Karp D, Camidge D, Infante J, Ames T, Price M, Jimeno J, Bryce A. Phase I study of PT-112, a novel pyrophosphateplatinum immunogenic cell death inducer, in advanced solid tumours. *Lancet eClinMed*. 2022;49:101430.
25. Karp D, Dronca R, Camidge R, Costello B, Mansfield A, Ames T, Jimeno J, Bryce A. Phase Ib dose escalation study of novel immunogenic cell death (ICD) inducer PT-112 plus PD-L1 inhibitor avelumab in solid tumours. *Ann Oncol*. 2020;31:5708.
26. Yim C, MT C, Johnson H, Mancini M, Stossi F, Mancini M, Azofeifa J, Price M, Baeck J, Ames T. PT-112, a novel immunogenic cell death (ICD) inducer, causes nucleolar stress leading to ribosomal biogenesis inhibition in cancer cells. AACR-NCU-EORTC International Conference Poster C128 2023.
27. Soler-Agesta R, Guilbaud E, Sato A, Yamazaki T, Yim C, Congenie M, Price M, Ames T, Anel A, Galluzzi L. Molecular mechanisms of immunogenic cell death driven by PT-112. *J Immunother Cancer*. 2023;11. <https://doi.org/10.1136/jitc-2023-SITC2023.1106>.
28. Soler-Agesta R, Marco-Brualla J, Minjárez-Sáenz M, Yim C, Martínez-Júlvez M, Price M, Moreno-Loshuertos R, Ames T, Jimeno J, Anel A. PT-112 induces mitochondrial stress and immunogenic cell death, targeting Tumor cells with mitochondrial deficiencies. *Cancers*. 2022;14:3851.
29. Yamazaki T, Galluzzi L, Yim C, Ames T. Immunologically relevant effects of PT-112 on cancer cell mitochondria. *J Immunother Cancer*. 2022;10(Suppl 2):A1160.
30. Yamazaki T, Buqué A, Ames T, Galluzzi L. PT-112 induces immunogenic cell death and synergizes with immune checkpoint blockers in mouse tumor models. *Oncol Immunol*. 2020;9:e1721810.
31. McAdams M, Swift S, Donahue R, Celades C, Tsai Y, Bingham M, Szabo E, Zhao C, Sansone S, Choradia N, et al. Preliminary efficacy, safety, and immunomodulatory effects of PT-112 from a phase 2 proof of concept study in patients with thymic epithelial tumors. *J Clin Oncol*. 2023;41(supplementS):e20647.
32. McAdams M, Swift S, Donahue R, Celades C, Tsai Y, Bingham M, Szabo E, Zhao C, Sansone S, Feierabend C, et al. Phase 2 clinical trial of PT-112 in patients with thymic epithelial tumors. *Mediastinum*. 2023;7:AB016.
33. Ames T, Sharik M, Rather G, Hochart G, Bonnel D, Linehan S, Stauber J, Wing R, Jimeno J, Medina D, et al. Translational research of PT-112, a clinical agent in advanced phase I development: evident bone tropism, synergy in vitro with bortezomib and lenalidomide, and potent efficacy in the Vk*MYC mouse model of multiple myeloma. *Blood*. 2017;130:1797.
34. Nishimura K. Management of bone metastasis in prostate cancer. *J Bone Min Metab*. 2023;41:317–26.
35. Marco-Brualla J, Al-Wasaby S, Soler R, Romanos E, Conde B, Justo-Méndez R, Enríquez J, Fernández-Silva P, Martínez-Lostao L, Villalba M, et al. Mutations in the ND2 subunit of mitochondrial complex I are sufficient to confer increased tumorigenic and metastatic potential to cancer cells. *Cancers*. 2019;11(7):1027.
36. Dong L, Neuzil J. Targeting mitochondria as an anticancer strategy. *Cancer Commun*. 2019;39:63.
37. Sainero-Alcolado L, Liaño-Pons J, Ruiz-Pérez M, Arsenian-Henriksson M. Targeting mitochondrial metabolism for precision medicine in cancer. *Cell Death Differ*. 2022;29:1304–17.
38. Lee Y, Park D, Chae Y. Role of mitochondrial stress response in Cancer Progression. *Cells*. 2022;11:771.
39. Jin P, Jiang J, Zhou L, Huang Z, Nice E, Huang C, Fu L. Mitochondrial adaptation in cancer drug resistance: prevalence, mechanisms, and management. *J Hematol Oncol*. 2022;15:97.
40. Onukwufor J, Berry B, Wojtovich A. Physiologic implications of reactive oxygen species production by Mitochondrial Complex I Reverse Electron Transport. *Antioxidants*. 2019;8:285.
41. Acín-Pérez R, Fernández-Silva P, Peleato M, Pérez-Martos A, Enríquez J. Respiratory active mitochondrial supercomplexes. *Mol Cell*. 2008;32:529–39.
42. Schagger H, Pfeiffer K. Supercomplexes in the respiratory chains of yeast and mammalian mitochondria. *Embo J*. 2000;19(8):1777–83.
43. Lapuente-Brun E, Moreno-Loshuertos R, Acín-Pérez R, Latorre-Pellicer A, Colás C, Balsa E, Perales-Clemente E, Quirós P, Calvo E, Rodríguez-Hernández M, et al. Supercomplex assembly determines electron flux in the mitochondrial electron transport chain. *Science*. 2013;340:1567–70.
44. Karp D, Camidge D, Infante J, Ames T, Jimeno J, Bryce A. A well-tolerated novel immunogenic cell death (ICD) inducer with activity in advanced solid tumors. *Ann Oncol*. 2018;29:viii143.
45. Marchetti P, Fovez Q, Germain N, Khamari R, Kluz J. Mitochondrial spare respiratory capacity: mechanisms, regulation, and significance in non-transformed and cancer cells. *FASEB J*. 2020;34:13106–24.
46. Hill B, Benavides G, Lancaster J, Ballinger S, Dell'Italia L, Jianhua Z. VM D-U: integration of cellular bioenergetics with mitochondrial quality control and autophagy. *Biol Chem*. 2012;393:1485–512.
47. Chen Q, Vazquez E, Moghaddas S, Hoppel C, Lesnefsky E. Production of reactive oxygen species by Mitochondria. CENTRAL ROLE OF COMPLEX III. *J Biol Chem*. 2003;278:36027–31.
48. Nakamura H, Takada K. Reactive oxygen species in cancer: current findings and future directions. *Cancer Sci*. 2021;112:3945–52.
49. Lee S, Son J, Lee J, Cheong H. Unraveling the intricacies of Autophagy and Mitophagy: implications in Cancer Biology Cells. 2023;12:2742.

50. Serrano-Del Valle A, Anel A, Naval J, Marzo I. Immunogenic cell death and immunotherapy of multiple myeloma. *Front Cell Dev Biol.* 2019;7:50.
51. Gupta G, Borgium K, Chen H. Immunogenic cell death: a step ahead of Autophagy in Cancer Therapy. *J Cancer Immunol.* 2021;3:47–59.
52. Kourelis T, Ailawadhi S, Vogl D, Cooper D, Ames T, Yim C, Price M, Jimeno J, Bergsagel P. A phase I dose escalation study of PT-112 in patients with relapsed or refractory multiple myeloma. *Blood.* 2020;Suppl 1136. <https://doi.org/10.1182/blood-2020-134916>.
53. Tang D. Understanding and targeting prostate cancer cell heterogeneity and plasticity. *Semin Cancer Biol.* 2022;82:68–93.
54. Galluzzi L, Kepp O, Hett E, Kroemer G, Marincola F. Immunogenic cell death in cancer: concept and therapeutic implications. *J Transl Med.* 2023;21:162.
55. Song Y, Zhou Y, Zhou X. The role of mitophagy in innate immune responses triggered by mitochondrial stress. *Cell Commun Signal.* 2020;18:186.
56. Vringer E, Tait S. Mitochondria and cell death-associated inflammation. *Cell Death Differ.* 2022;30:304–12.
57. Filomeni G, De Zio D, Cecconi F. Oxidative stress and autophagy: the clash between damage and metabolic needs. *Cell Death Differ.* 2015;22:377–88.
58. Roca-Agujetas V, de Dios C, Lestón L, Marí M, Morales A, Colell A. Recent Insights into the Mitochondrial Role in Autophagy and Its Regulation by Oxidative Stress. *Oxid Med Cell Longev.* 2019;3809308.
59. Galluzzi L, Kepp O, Hett E, Kroemer G, Marincola F. Immunogenic cell death in cancer: concept and therapeutic implications. *J Transl Med* 2023.
60. Yamazaki T, Kirchmair A, Sato A, Buqué A, Rybstein M, Petroni G, Bloy N, Finotello F, Stafford L, Navarro Manzano E, et al. Mitochondrial DNA drives abscopal responses to radiation that are inhibited by autophagy. *Nat Immunol.* 2020;21:1160–71.
61. Wang Z, Gall J, Bonegio R, Havasi A, Illanes K, Schwartz J, Borkan S. Nucleophosmin, a critical Bax cofactor in ischemia-induced cell death. *Mol Cell Biol.* 2013;33:1916–24.
62. Maehama T, Nishio M, Otani J, Mak T, Suzuki A. Nucleolar stress: molecular mechanisms and related human diseases. *Cancer Sci.* 2023;114:2078–86.
63. Kim J, Kim H, Chung J. Molecular mechanisms of mitochondrial DNA release and activation of the cGAS-STING pathway. *Exp Mol Med.* 2023;55:510–9.
64. Kwon J. S Bakhom 2020 The cytosolic DNA-Sensing cGAS-STING pathway in Cancer. *Cancer Discov* 10 26–39.
65. Pfister A. Emerging role of the nucleolar stress response in Autophagy. *Front Cell Neurosci.* 2019;13:156.
66. Quin J, Devlin J, Cameron D, Hannan K, Pearson R, Hannan R. Targeting the nucleolus for cancer intervention. *Biochim Biophys Acta.* 2014;1842:802–16.
67. Gilles A, Frechin L, Natchiar K, Biondani G, von Loeffelholz O, Holvec S, Malaval J, Winum J, Klaholz B, Peyron J. Targeting the human 80S ribosome in Cancer: from structure to function and Drug Design for innovative adjuvant therapeutic strategies cells 2020;9:629.

Publisher's note

Springer Nature remains neutral with regard to jurisdictional claims in published maps and institutional affiliations.